

## TITLE

Direct measurement of thermal conductivity in solid iron at planetary core conditions

## AUTHORS AND AFFILIATIONS

Zuzana Konôpková\*<sup>1</sup>, R. Stewart McWilliams\*<sup>2</sup>, Natalia Gómez-Pérez\*<sup>2,3</sup>, Alexander F. Goncharov\*<sup>4,5</sup>

<sup>1</sup> DESY Photon Science, Notkestrasse 85, DE-22607 Hamburg, Germany†

<sup>2</sup> School of Physics and Astronomy and Centre for Science at Extreme Conditions, University of Edinburgh, Peter Guthrie Tait Road, Edinburgh, UK EH9 3FD

<sup>3</sup> Departamento de Geociencias, Universidad de Los Andes, Bogotá, Colombia

<sup>4</sup> Key Laboratory of Materials Physics, Institute of Solid State Physics, Chinese Academy of Sciences, 350 Shushanghu Road, Hefei, Anhui 230031, China

<sup>5</sup> Geophysical Laboratory, Carnegie Institution of Washington, 5251 Broad Branch Road NW, Washington DC, 20015, USA

\*corresponding authors

† now at European XFEL GmbH, Notkestrasse 85, DE-22607 Hamburg, Germany

## TEXT

**The conduction of heat through minerals and melts at extreme pressures and temperatures is of central importance to the evolution and dynamics of planets. In the cooling Earth's core, the thermal conductivity of iron alloys defines the adiabatic heat flux and thus, the thermal and compositional energy available to support the production of Earth's magnetic field via dynamo action<sup>1-3</sup>. Attempts**

**to describe thermal transport in Earth's core have been problematic, with predictions of high thermal conductivity<sup>4-7</sup> at odds with traditional geophysical models and direct evidence for a primordial magnetic field<sup>8-10</sup>. Direct measurements of core heat transport are now vital to firmly resolve this enigma. In this study, we present direct measurements of the thermal conductivity of solid iron at pressure and temperature conditions relevant to the cores of planets ranging in size from Mercury to Earth, using the dynamically laser-heated diamond-anvil cell<sup>11,12</sup>. Our measurements place the thermal conductivity of Earth's core near the low end of previous estimates, at 18-44 W/m/K. The result is in agreement with paleomagnetic measurements<sup>10</sup> that find Earth's geodynamo has persisted since the earliest eon of Earth history, and allows for a solid inner core as old as the dynamo.**

The thermal evolution of the Earth's core and the energetics of the geomagnetic field are highly sensitive<sup>3,8,9</sup> to the thermal conductivity of core materials at relevant high pressures ( $P$ ) and high temperatures ( $T$ ). A wide range of values for the thermal conductivity of iron and its alloys at core conditions have been predicted using materials theory<sup>2,4,6,7,13</sup> and high-pressure measurements of electrical conductivity<sup>5,14-16</sup>. To predict thermal conductivity, the Wiedemann-Franz-Lorenz law

$$k = LT\sigma \quad (1)$$

has almost universally been employed, where  $k$  and  $\sigma$  are the thermal and electrical conductivities and  $L$  is the Lorenz number. The Lorenz number — traditionally an empirically determined quantity<sup>17</sup> — has been calculated theoretically<sup>6,7</sup> but not measured for iron or its alloys at high  $P$ - $T$  conditions.

For low estimates of thermal conductivity<sup>2</sup>, near  $k = 30$  W/m/K, the geodynamo may be sustained during the whole life of the planet, and convection of the core is readily attained in thermal (in absence of an inner core) or thermochemical scenarios<sup>9</sup>. On the other hand, a recent estimate<sup>6</sup> near  $k = 130$  W/m/K, implies a young inner core (i.e. less than 1.3 Gyr old), and only thermal convection driving the dynamo at earlier times<sup>3</sup>. However, a paradox arises<sup>8</sup> when evidence of an ancient magnetic field<sup>3,10</sup> must be reconciled with the high energy fluxes needed to drive thermal convection in a high conductivity, fully fluid core. The large core-mantle boundary heat flux ( $Q_{CMB}$ ) and high internal temperatures for the early Earth in this case (implying a molten lower mantle and possibly stably-stratified core) are difficult to explain given current mantle evolution models and low present day<sup>3</sup>  $Q_{CMB}$ . Re-evaluating the history and energy balances of Earth's core and mantle in this context, it is necessary to have certainty on the validity of reported values of  $k$  (Ref. 8). Thus, there is a pressing need for direct thermal conductivity measurements of core materials at conditions relevant to the Earth's core.

While the technical capability of reaching planetary core conditions in the laboratory has long been available using the laser-heated diamond anvil cell, measurements sensitive to transport properties have been scarce. Thermal transport measurements have been especially challenging. To overcome this limitation, we dynamically measured temperature in the laser heated diamond anvil cell<sup>11,12</sup> to study the propagation of heat pulses across iron foils contained at high initial pressure (35-130 GPa) and temperature (1600-3000 K) (Fig. 1). Fitting of temporally and spatially resolved temperature fluctuations with heat conduction models provides a strong constraint on the thermal transport (Methods and Extended Data Figs. 2-6).

The experiments performed below  $\sim 50$  GPa probe Fe in the stability field of fcc  $\gamma$ -Fe (Fig. 2)<sup>18-22</sup>. At conditions close to those at the centre of Mercury's core<sup>23</sup> ( $\sim 40$  GPa and 2200-2500 K), thermal conductivity is  $35 \pm 10$  W/m/K. This is similar to the ambient pressure values in  $\gamma$ -Fe ( $k = 30 \pm 3$  W/m/K)<sup>24</sup> suggesting  $k$  is not strongly dependent on pressure at Mercury's core conditions. This result is similar to earlier expectations for the thermal conductivity of Mercury's core<sup>25</sup> of  $\sim 40$  W/m/K, but is at odds with more recent estimates<sup>21</sup>. At pressures between 50-80 GPa, the sample is usually pre-heated in the hcp  $\epsilon$ -Fe phase but may undergo partial transformation to the  $\gamma$  phase during the thermal pulse<sup>18</sup>. Thermal conductivity values found at these conditions are considered biased toward the  $\epsilon$ -phase, and are in general agreement with earlier DAC measurements on  $\epsilon$ -Fe<sup>26</sup>. The highest pressure data, from 88-130 GPa and 1600-3500 K, are unambiguously in the region of  $\epsilon$ -Fe and are closest to conditions at Earth's core-mantle boundary<sup>1,6</sup> (CMB): 136 GPa and 3800-4800 K. A large number of measurements ( $> 20$ ) at 112 GPa show  $k$  to decrease with temperature at these conditions (Fig. 3), as previously inferred from combining electrical conductivity data under static and shock wave compression<sup>14</sup>.

To model the temperature dependence of thermal conductivity in  $\epsilon$ -Fe, we fit the data at 112 GPa to

$$k = aT + \frac{b}{\sqrt{T}} \quad (2)$$

This form ensures a realistic behaviour of both thermal conductivity and electrical resistivity ( $1/\sigma$ ) that is consistent with previous high-temperature resistivity data<sup>5,14,21</sup> (see Methods and Extended Data Fig. 1). The model fit at 112 GPa (Fig. 3) included also resistivity data at room temperature<sup>5,14</sup> extrapolated to 112 GPa and shock wave resistivity data<sup>15</sup> interpolated to 112 GPa. These were converted to thermal

conductivity using an empirical Lorenz number of  $1.9(0.4) \times 10^{-8} \text{ W}\Omega\text{K}^{-2}$  (see Methods). The fit of Eq. 2 yields  $b \approx 1972 \text{ W/m/K}^{1/2}$  and  $a \approx 0$ . Error in model thermal conductivities is  $\sim 20\%$  ( $1\sigma$ ).

To assess the pressure variation of  $k$  in  $\epsilon$ -Fe, we use a physical model for the variation of electronic thermal conductivity with pressure (see Methods) in terms of isothermal bulk modulus ( $K_T$ ) and Grüneisen parameter ( $\gamma$ )

$$\frac{1}{k} \frac{\partial k}{\partial P} = \frac{2\gamma - 1/3}{K_T} \quad (3)$$

The Grüneisen parameter and bulk modulus at core conditions are evaluated using the thermal equation of state of iron<sup>27</sup> (see Methods). The model represents our data well to 130 GPa (Fig. 2), and predicts somewhat larger values of  $k$  at Earth's outer core conditions (Fig. 3). Accounting for the uncertainty in outer core temperature<sup>1,6</sup>,  $k$  for pure iron varies from  $33 \pm 7 \text{ W/m/K}$  at CMB conditions ( $T=3800\text{-}4800 \text{ K}$ ,  $P=136 \text{ GPa}$ ) to  $46 \pm 9 \text{ W/m/K}$  at inner core boundary (ICB) conditions ( $T=5600\text{-}6500 \text{ K}$ ,  $P=330 \text{ GPa}$ ).

The conductivity of molten Fe, as relevant to the outer core, is generally taken to be similar to the solid near melting<sup>13,21,28</sup>. Addition of light-element impurities is expected to reduce conductivity by 10-40%<sup>7,13</sup>. Thus, the thermal conductivity for Earth's liquid outer core is between  $25 \pm 7 \text{ W/m/K}$  at the CMB and  $35 \pm 10 \text{ W/m/K}$  at the ICB. Refining estimates for liquid core composition can further reduce this uncertainty. The corresponding electrical resistivity of the outer core is  $3.7 \pm 1.5 \mu\Omega\text{m}$ .

Our thermal conductivities for iron at core conditions compare well with predictions based on resistivity measurements at high pressure<sup>14</sup> ( $52 \pm 11 \text{ W/m/K}$ ) or Stacey's law of constant resistivity at melting<sup>2</sup> ( $48 \pm 10 \text{ W/m/K}$ ), where the empirical

value of  $L$  has been applied. Such predictions are very sensitive to the assumptions used, however, and significantly larger values are found using slightly different approaches<sup>5,13,14</sup>, emphasizing the need for direct constraints from high pressure-temperature data. Calculations<sup>6,7</sup> finding  $k = 120\text{-}160$  W/m/K at CMB and  $k = 205\text{-}250$  W/m/K at ICB conditions are  $5.6\pm 1.8$  and  $6.5\pm 1.7$  times larger than our values, respectively.

During an early stage of Earth history before the formation of the inner core, the presence of the geodynamo requires a core-mantle boundary heat flux ( $Q_{CMB}$ ) greater than the conductive heat flux in the core. The heat flux requirements for such a convective early core are moderate for the values of  $k$  found in this study, similar to Ref. 9:  $Q_{CMB}$  must exceed a threshold of  $3.8\pm 1.6$  TW (for  $k$  of  $31\pm 13$  W/m/K) for Earth's magnetic field to be sustained, assuming negligible radiogenic heating. Later in the planet's history, after a solid inner core has formed, the core-mantle heat flux necessary to sustain a dynamo may be smaller, given that convection can be driven both compositionally and thermally. Estimates<sup>3</sup> for the current  $Q_{CMB}$  ( $12\pm 5$  TW) far exceed this threshold, so for a nominal scenario of  $Q_{CMB}$  declining or constant with time<sup>3,9</sup> magnetic activity is expected throughout Earth history, and would likely only have been absent when internal dynamics differed substantially from present, for example in periods lacking plate tectonics<sup>29</sup>. Similarly, evidence of non-zero paleomagnetic field places a hard constraint on the corresponding heat flux of  $Q_{CMB} > 2.2$  TW prior to inner core nucleation.

However, the inner core can be older for lower core thermal conductivities<sup>5</sup>, and within the uncertainty due to core light element content, the inner core can be as old as the earliest recorded terrestrial magnetic field<sup>10</sup>, i.e., up to 4.2 Gyr. That is, within our direct experimental constraints, there is no requirement that Earth's

geodynamo ever existed in the absence of an inner core. Indeed, the planet's dynamo and its solid inner core may have co-existed since the formation of Earth. Greater knowledge of core light element content and its effect on thermal conductivity is essential to further understand this earliest period of Earth's core evolution.

## REFERENCES

- 1 Labrosse, S. Thermal and magnetic evolution of the Earth's core. *Phys. Earth Planet. Inter.* **140**, 127-143 (2003).
- 2 Stacey, F. D. & Loper, D. E. A revised estimate of the conductivity of iron alloy at high pressure and implications for the core energy balance. *Phys. Earth Planet. Inter.* **161**, 13-18 (2007).
- 3 Nimmo, F. in *Treatise on Geophysics (Second Edition)* (ed Gerald Schubert) 27-55, 201-219 (Elsevier, 2015).
- 4 Sha, X. & Cohen, R. First-principles studies of electrical resistivity of iron under pressure. *Journal of Physics: Condensed Matter* **23**, 075401 (2011).
- 5 Gomi, H. *et al.* The high conductivity of iron and thermal evolution of the Earth's core. *Phys. Earth Planet. Inter.* **224**, 88-103 (2013).
- 6 Pozzo, M., Davies, C., Gubbins, D. & Alfe, D. Thermal and electrical conductivity of iron at Earth's core conditions. *Nature* **485**, 355-U399 (2012).
- 7 de Koker, N., Steinle-Neumann, G. & Vlcek, V. Electrical resistivity and thermal conductivity of liquid Fe alloys at high P and T, and heat flux in Earth's core. *Proc. Natl. Acad. Sci. U. S. A.* **109**, 4070-4073 (2012).
- 8 Olson, P. The New Core Paradox. *Science* **342**, 431-432 (2013).
- 9 Nimmo, F. in *Treatise on Geophysics* (ed Gerald Schubert) 31-65, 217-241 (Elsevier, 2007).
- 10 Tarduno, J. A., Cottrell, R. D., Davis, W. J., Nimmo, F. & Bono, R. K. A Hadean to Paleoproterozoic geodynamo recorded by single zircon crystals. *Science* **349**, 521-524 (2015).

- 11 McWilliams, R. S., Konôpková, Z. & Goncharov, A. F. A flash heating method for measuring thermal conductivity at high pressure and temperature: application to Pt. *Phys. Earth Planet. Inter.* **247**, 17-26 (2015).
- 12 McWilliams, R. S., Dalton, D. A., Konopkova, Z., Mahmood, M. F. & Goncharov, A. F. Opacity and conductivity measurements in noble gases at conditions of planetary and stellar interiors. *Proceedings of the National Academy of Sciences* **112**, 7925 (2015).
- 13 Stacey, F. D. & Anderson, O. L. Electrical and thermal conductivities of Fe-Ni-Si alloy under core conditions. *Phys. Earth Planet. Inter.* **124**, 153-162 (2001).
- 14 Seagle, C. T., Cottrell, E., Fei, Y. W., Hummer, D. R. & Prakapenka, V. B. Electrical and thermal transport properties of iron and iron-silicon alloy at high pressure. *Geophysical Research Letters* **40**, 5377-5381 (2013).
- 15 Bi, Y., Tan, H. & Jing, F. Electrical conductivity of iron under shock compression up to 200 GPa. *Journal of Physics: Condensed Matter* **14**, 10849 (2002).
- 16 Keeler, R. N. & Royce, E. B. in *Physics of High Energy Density* Vol. 48 (eds P Caldirola & H Knoepfel) 106-125 (Academic Press, 1971).
- 17 Franz, R. & Wiedemann, G. Ueber die Wärme-Leitungsfähigkeit der Metalle. *Annalen der Physik* **165**, 497-531 (1853).
- 18 Anzellini, S., Dewaele, A., Mezouar, M., Loubeyre, P. & Morard, G. Melting of Iron at Earth's Inner Core Boundary Based on Fast X-ray Diffraction. *Science* **340**, 464-466 (2013).
- 19 Boehler, R. Temperatures in the Earth's core from melting-point measurements of iron at high static pressures. *Nature* **363**, 534-536 (1993).

- 20 Komabayashi, T., Fei, Y., Meng, Y. & Prakapenka, V. In-situ X-ray diffraction measurements of the  $\gamma$ - $\epsilon$  transition boundary of iron in an internally-heated diamond anvil cell. *Earth and Planetary Science Letters* **282**, 252-257 (2009).
- 21 Deng, L., Seagle, C., Fei, Y. & Shahar, A. High pressure and temperature electrical resistivity of iron and implications for planetary cores. *Geophysical Research Letters* **40**, 33-37 (2013).
- 22 Jackson, J. M. *et al.* Melting of compressed iron by monitoring atomic dynamics. *Earth and Planetary Science Letters* **362**, 143-150 (2013).
- 23 Rivoldini, A., Van Hoolst, T. & Verhoeven, O. The interior structure of Mercury and its core sulfur content. *Icarus* **201**, 12-30 (2009).
- 24 Ho, C. Y., Powell, R. W. & Liley, P. E. Thermal Conductivity of the Elements. *Journal of Physical and Chemical Reference Data* **1**, 279-422 (1972).
- 25 Hauck, S. A., Dombard, A. J., Phillips, R. J. & Solomon, S. C. Internal and tectonic evolution of Mercury. *Earth and Planetary Science Letters* **222**, 713-728 (2004).
- 26 Konopkova, Z., Lazor, P., Goncharov, A. F. & Struzhkin, V. V. Thermal conductivity of hcp iron at high pressure and temperature. *High Pressure Research* **31**, 1-9 (2011).
- 27 Dubrovinsky, L. S., Saxena, S. K., Tutti, F., Rekhi, S. & LeBehan, T. In Situ X-Ray Study of Thermal Expansion and Phase Transition of Iron at Multimegabar Pressure. *Physical Review Letters* **84**, 1720-1723 (2000).

- 28 Secco, R. A. & Schloessin, H. H. The electrical resistivity of solid and liquid Fe at pressures up to 7 GPa. *Journal of Geophysical Research: Solid Earth* **94**, 5887-5894 (1989).
- 29 Nimmo, F. & Stevenson, D. J. Influence of early plate tectonics on the thermal evolution and magnetic field of Mars. *Journal of Geophysical Research: Planets* **105**, 11969-11979 (2000).

## ACKNOWLEDGEMENTS

The authors acknowledge experimental assistance from Hauke Marquardt, and constructive suggestions on this manuscript by three anonymous reviewers. This work was supported by the NSF Major Research Instrumentation program, NSF EAR-1015239, NSF EAR-1520648 and NSF EAR/IF-1128867, the Army Research Office (56122-CH-H), the Carnegie Institution of Washington, the National Natural Science Foundation of China, the National Natural Science Foundation of China (No. 21473211), the Chinese Academy of Science (Grant No. YZ201524), the University of Edinburgh, and the British Council Researcher Links Programme. Portions of this research were carried out at the light source Petra III at DESY, a member of the Helmholtz Association (HGF).

## AUTHOR CONTRIBUTIONS

ZK, RSM, and AFG designed and conducted experiments. RSM reduced raw data. ZK and NGP performed finite-element modelling. NGP performed error analysis and geophysical calculations. All authors wrote the manuscript.

## AUTHOR INFORMATION

Reprints and permissions information is available at [www.nature.com/reprints](http://www.nature.com/reprints). These authors declare no competing financial interests. Correspondence and requests for materials should be addressed to Z. K. (zuzana.konopkova@xfel.eu), R.S.M. (r.s.mcwilliams@ed.ac.uk), N. G-P. (ngomez@uniandes.edu.co), or A. F. G. (alex@issp.ac.cn).

FIGURE LEGENDS

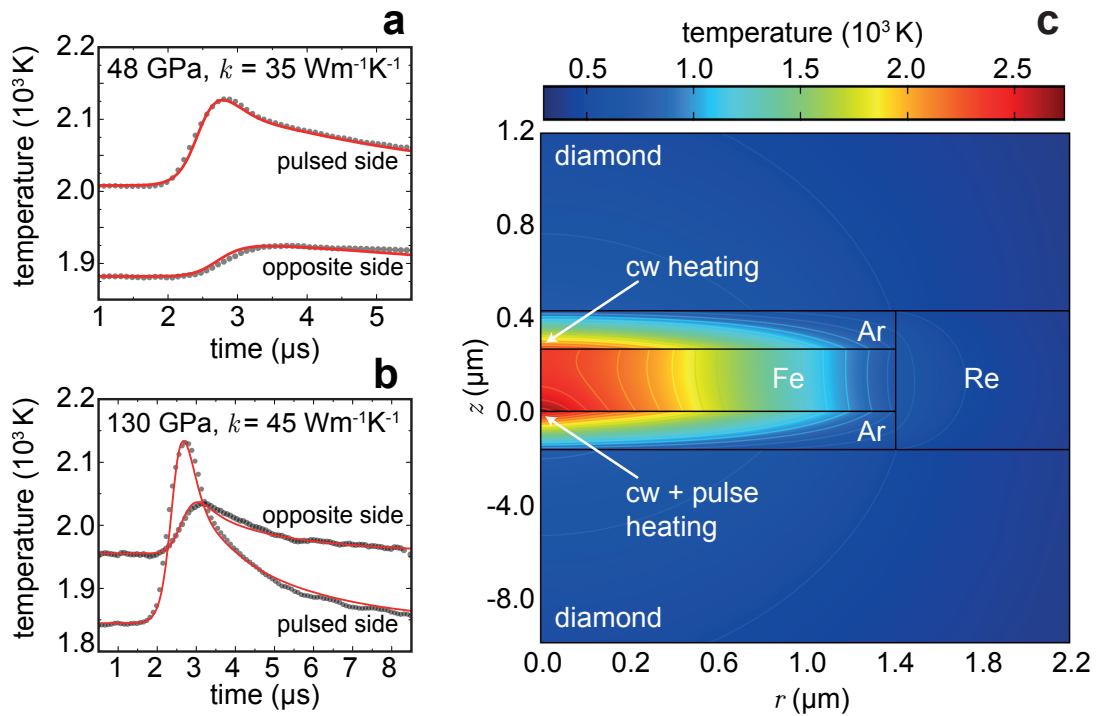


FIG. 1: Temperature of iron foils during flash heating at high initial temperature and pressure. **a** and **b**, Plot of the measured temperature histories (grey) on the pulsed and opposite sides of the foil together with finite-element models (red) for best-fit thermal conductivity, at two pressures: **a**,  $P=48$  GPa and **b**,  $P=130$  GPa. **c** Instantaneous temperature map of the modelled sample area at initiation of flash heating at 112 GPa, as a function of radial ( $r$ ) and axial ( $z$ ) position. Contour lines are isotherms.

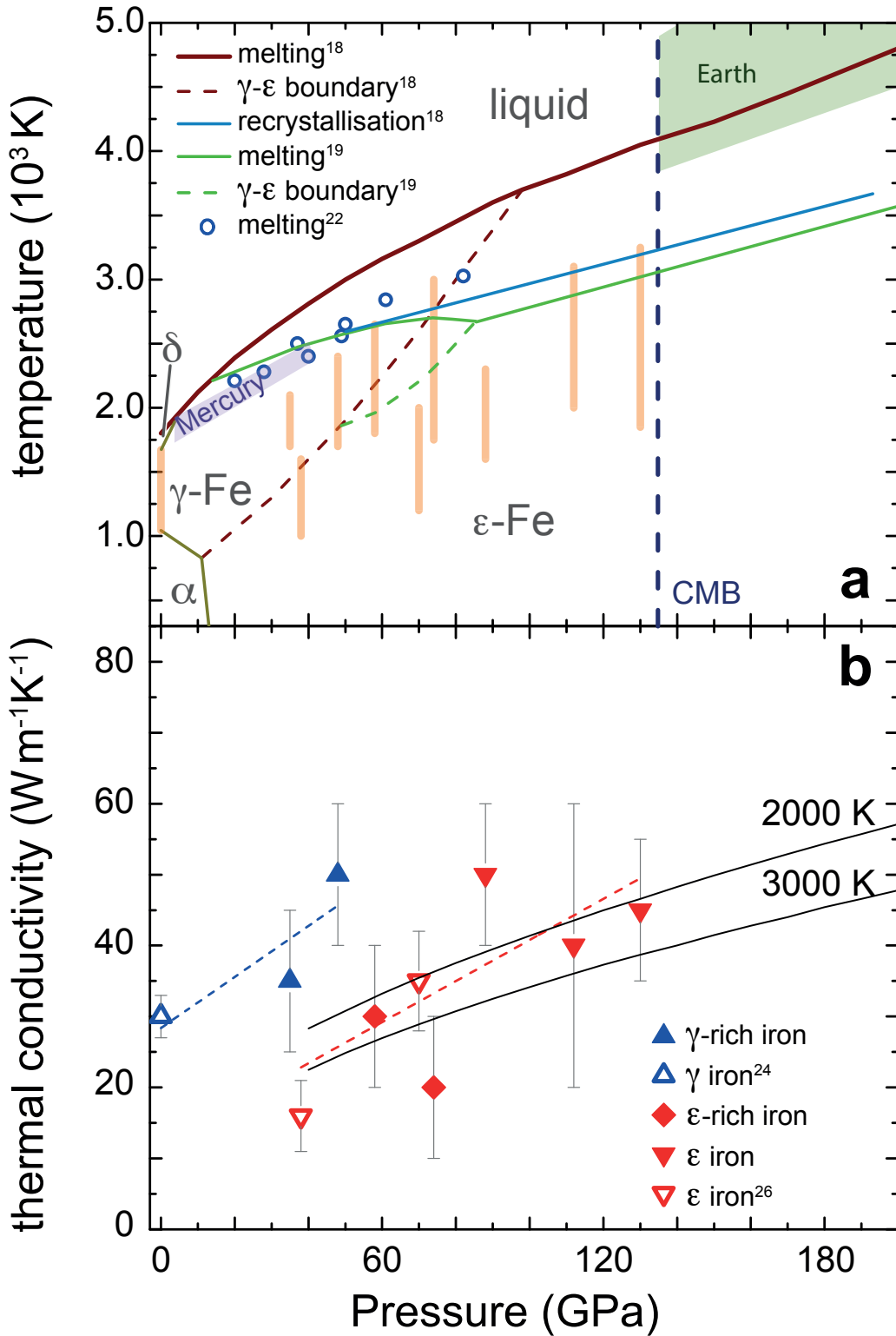


FIG. 2: Thermal conductivity of iron at high pressure and temperature. **a** Phase diagram of iron<sup>18-20,22</sup> with conditions of thermal conductivity measurements (orange) falling in the domain of the  $\gamma$ - and  $\epsilon$ -phases. The shaded areas depict conditions of

Earth's<sup>1,6</sup> and Mercury's<sup>23</sup> cores, with the vertical dashed line marking the pressure at Earth's core mantle boundary. **b** Thermal conductivity results from this study are solid symbols: in the domain of  $\gamma$ -Fe (upward triangles),  $\gamma$  and  $\epsilon$  phases most likely co-exist<sup>18</sup>; for samples typically pre-heated to below the  $\gamma$ - $\epsilon$  boundary which crossed it briefly during thermal pulses (diamonds), samples are considered to be mostly  $\epsilon$ -Fe; at higher pressure (downward triangles) samples are pure  $\epsilon$ -Fe at all conditions<sup>18</sup> (see Methods). Prior direct thermal conductivity measurements on  $\gamma$ -<sup>24</sup> and  $\epsilon$ -phases<sup>26</sup> are open symbols. The dashed lines are linear fits to  $\gamma$ - and  $\epsilon$ -domain results, whereas solid lines are model values (Eqs. 2-3). Error bars include uncertainty (1 SD) and range of measurements.

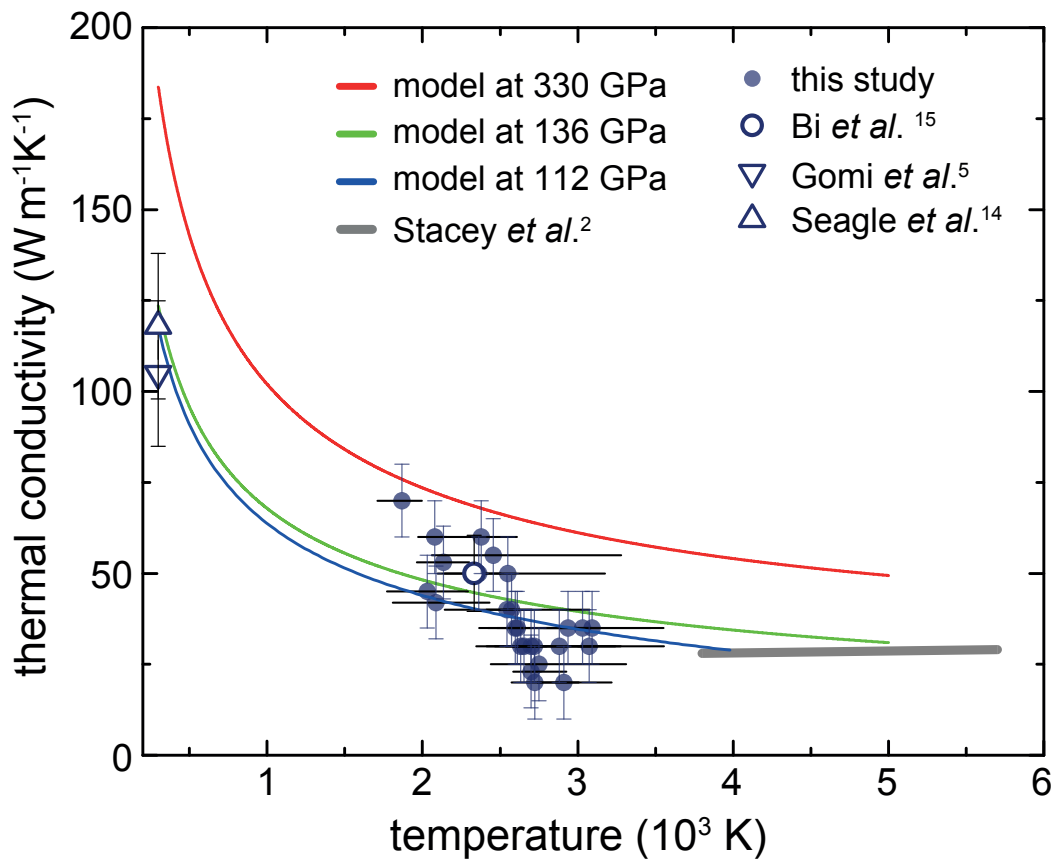


FIG. 3: Thermal conductivity of iron versus temperature. Solid circles are from this study at 112 GPa, with horizontal bars indicating the range of temperatures observed in each experiment, and vertical bars the uncertainty in  $k$  (1 SD). Estimates based on prior electrical resistivity measurements<sup>5,14,15</sup> are open symbols, with bars indicating uncertainty from the empirical determination of  $L$ . The thermal conductivity model for 112 GPa, 136 GPa (CMB), and 330 GPa (ICB) are blue, green and red, respectively (Eqs. 2-3). For comparison, the prediction of Ref. 2 for core alloy at outer core conditions is the grey line.

## METHODS

### Brief Methods

A high-purity iron foil (99.99%, GoodFellow Corp.) placed between two anvils of the diamond cell and separated from the anvils by layers of insulating material (NaCl or Ar) was preheated using a continuous laser to a desired stable temperature using double-sided continuous wave (CW) IR laser heating, and then pulse heated on one side with an additional IR laser to create a thermal disturbance<sup>11</sup>. The evolution of this disturbance was characterized by nanosecond-resolved radiative temperature measurements using a streak camera coupled to a grating spectrograph that records the thermal incandescent history from both sides of the foil. The phase shift and the reduction in amplitude of the temperature disturbance as it propagates across the foil are thus measured<sup>11</sup>. At a given pressure, a series of datasets were collected using different CW and pulse laser powers. Temperatures studied ranged from ~1600 K, the lowest detectable temperature, to 4000 K at the maximum, whereas temperature disturbances were typically a few hundred K in amplitude.

The temperature evolution was fit to time-dependent finite element models of the laser heated diamond cell<sup>11,26,30</sup> to determine thermal conductivity of iron samples. Finite element modelling employed experimentally determined geometrical parameters and thermochemical parameters determined from known equations of state. Thermal conductivity of the sample, together with thermal conductivity of the pressure medium and heating power, are adjusted until the best match of modelled and experimental temperature is achieved (Fig. 1a). The analysis was rigorously tested for sensitivity to input parameters (Extended Data Figs. 2, 3 and 6). Total uncertainty and error bars (Fig. 2) were determined from fitting uncertainty (Extended Data Figs. 2, 5), the scatter across different datasets (e.g. Fig. 3), and uncertainty in

input parameters (Extended Data Figs. 3, 6). We find the measurements to be sufficiently sensitive to thermal conductivity of the sample foil to provide a major constraint on Fe conductivity at core conditions.

Experiment duration (0.1 to 10 s per temperature history collection) was kept as short as possible to avoid sample damage and minimize heating of optics and DAC that could cause instabilities during long laser heating runs.

Foil initial thickness ( $4.01 \pm 0.02 \mu\text{m}$ ) and *in-situ* thickness (Extended Data Table 1) were measured using white light interferometry of the diamond cell, and index of refraction data for the media under pressure<sup>31-33</sup>; these measurements also determined the sample to diamond culet distances which are important parameters in finite element calculations. Foil thickness changes measured under compression were consistent with those derived from the known equation of state of Fe<sup>34</sup>. For NaCl medium, insulation plates were formed and placed on the culets, and foils were placed between them; in the case of Ar, the foil was suspended on a recess in the gasket (Re).

A sample of platinum, which has well-defined thermal conductivity behaviour<sup>11</sup> at high  $P$ - $T$ , was available as a control in some experiments at low pressures where DAC cavities were sufficiently large in diameter ( $P \leq 55 \text{ GPa}$ ) to accommodate a second foil. The Pt foil had the same thickness as the Fe foil, and was positioned on the plane of the Fe foil in the cavity; for such foil pairs, sample and insulation thicknesses, cell geometry, pressure, medium, heating configuration, and detection system were identical, allowing for a direct relative comparison between the thermal transport behaviour of the two materials. Heat wave propagation across the platinum was significantly faster than in Fe (e.g. 240 ns for the half rise-time, compared to 565 ns in Fe at 48 GPa, Extended Data Fig. 4), corresponding to a lower

thermal diffusivity for Fe. Fe samples were also observed to sustain larger axial temperature gradients than the Pt samples, manifested in a greater difference between peak amplitudes on either side of the foil. These observations affirm that at the studied conditions, thermal conductivity of Pt<sup>11</sup> ( $160 \pm 40$  W/mK) is significantly greater than that of Fe.

The Lorenz number for  $\epsilon$ -Fe was determined by comparing shock wave electrical resistivity<sup>15</sup> and the present thermal conductivity data at comparable pressure and temperature (Fig. 3). The result is 22(16)% lower than the value for a free-electron metal<sup>35</sup> ( $L = 2.44 \times 10^{-8}$  W $\Omega$ K<sup>-2</sup>), consistent with theoretical expectations<sup>7</sup> which predict a Lorenz number reduced from the ideal by up to 17%.

### Experimental Details

To generate thermal perturbations at high initial pressure and temperature, we combined double-sided continuous and single-sided pulsed laser heating of the diamond anvil cell sample<sup>11</sup>. The initial temperature was reached by balancing laser power to either side of the sample until temperatures agreed to within  $\sim 100$  K, and then pulsed heating was used to create a small perturbation in temperature which propagated across the sample. Our approach is similar to that used in traditional flash heating measurements of thermal diffusivity<sup>36</sup>, modified for a specimen under pressure in a DAC<sup>11</sup>. The reduction in amplitude and phase shifting of the heat pulse with distance is an essentially one-dimensional phenomenon<sup>11,36</sup>, whereas two-dimensional effects have a secondary, but non-negligible, impact accounted for via finite-element modelling.

Precise temperature determination during pulse laser heating was made with a streak camera detecting system coupled to a spectrometer, capable of detecting

thermal emission in a time-resolved manner in a spectrogram. Three to ten microsecond spectrograms are synchronized to the heating pulses to follow the sample's temperature response on both sides. Thermal emission was fit to a greybody Planck function assuming constant emissivity during the heat cycle<sup>11</sup>, a reasonable approximation since thermal perturbations are small. The time resolution of the temperature measurements was 26 ns (3  $\mu$ s sweep) to 82 ns (10  $\mu$ s sweep). Spectrograms were integrated over  $10^2$  to  $10^4$  perturbation cycles, at a rate of 1 kHz and total integration times of 0.1 to 10 seconds, the total integration time depending on temperature. Emission was calibrated to a tungsten ribbon lamp of known radiance. Temperatures were detected only above  $\sim 1600$  K due to lack of signal at lower temperatures. Experiments were limited at high temperatures due to visible foil deformation in the melting regime of sample and pressure medium<sup>11</sup>.

Thermal pressures produced during laser heating are positive but small (of order a few GPa) in sample configurations similar to those used here<sup>18</sup> and do not significantly affect our results.

At pressures and temperatures in the stability field of  $\gamma$ -Fe, fcc  $\gamma$ -Fe and hcp  $\epsilon$ -Fe are commonly observed to coexist in experiments<sup>18</sup>. Consequently, our data at these conditions may probe a mixed  $\gamma$ -,  $\epsilon$ -Fe state with a variable  $\gamma$ -Fe composition (Fig. 2). In contrast, at higher pressures,  $\epsilon$ -Fe is typically the only observed solid phase at all temperatures<sup>18,37</sup>, so our data in this regime directly probe pure  $\epsilon$ -Fe. To test these expectations, we have also performed *in-situ* x-ray diffraction measurements on laser heated Fe samples prepared in a manner identical to that employed in this study (with NaCl media), at the P02.2 beamline (ECB) of PETRA III. Using comparable timescales of heating, we confirm that a mixed phase should be

present in lower-pressure experiments reported in this study, but not at higher pressures.

To prevent the uptake of impurities in our initially high-purity Fe foils, pressure medium materials (NaCl, Ar) were chosen and carefully prepared so that reactions with the sample are avoided<sup>38,39</sup>. During preparation, Fe foils and NaCl media and were kept dry, and contact with atmosphere was minimised to prevent foil oxidation. Carbon from diamond anvils is known to react with Fe at high pressures and temperatures in LHDAC experiments, but generally at significantly higher temperatures (and longer timescales) than probed in this work<sup>18,37</sup>. We have tested our sample preparation technique in our separate *in-situ* laser-heated DAC x-ray diffraction experiments, ruling out oxidation or reaction with the medium, and confirming that carbide formation occurs at significantly higher temperatures and longer heating timescales than we have used here. Thus our Fe samples should remain highly pure at the pressures, temperatures, and timescales of this study. Analysis of the recovered sample from experiments at 58-74 GPa using electron imaging, EDS (Energy Dispersive Scattering) for chemical analysis, and FIB (Focused Ion Beam) to section the foil at heated regions found no detectable local enrichment of light elements in the heated areas of the sample, indicating bulk impurity levels well below detection limits ( $\lesssim 0.6$  wt. % C,  $\lesssim 0.6$  wt. % O,  $\lesssim 100$  ppm Ar), consistent with expectations from x-ray diffraction. Finally, no systematic changes in measured conductivities were observed with heating time, indicating samples did not undergo any progressive transformation (e.g. reaction) that influenced the thermal conductivity.

Model for pressure variation of thermal conductivity.

The model used here to estimate pressure variation of thermal conductivity (Eq. 3) is based on a formal differentiation of the electronic thermal resistivity ( $W_e = l/k_e$ ) with respect to density combined with the definition of the Grüneisen parameter ( $\gamma = (\partial \ln \theta_D / \partial \ln \rho)_T$ ,  $\theta_D$  - Debye temperature,  $\rho$  - density), which leads to<sup>40</sup>

$$\left(\frac{\partial \ln W_e}{\partial \ln \rho}\right)_T = -2\gamma + \left(\frac{\partial \ln C}{\partial \ln \rho}\right)_T \quad (S1)$$

where  $C$  is a constant containing lattice and band structure information originating from the Bloch-Grüneisen expression. Bohlin<sup>41</sup> finds  $(\partial \ln C / \partial \ln \rho)_T$  being equal to -1/3 in ordinary pure metals and then the variation of electronic thermal conductivity with pressure can be expressed in terms of isothermal bulk modulus ( $K_T$ ) and Grüneisen parameter ( $\gamma$ ) as Eq. 3.

The Grüneisen parameter of iron is fairly well known at room  $T$ , high  $P$  – the data of Sharma<sup>42</sup> and Dubrovinsky et al.<sup>43</sup> agree well, particularly above 100 GPa. At core conditions (high  $T$ ),  $\gamma(P, T)$  and  $K_T(P, T)$  were evaluated using a thermal equation of state of iron<sup>27</sup>, with  $\gamma = \gamma_0 \left(\frac{V}{V_0}\right)^q$ , where  $\gamma_0 = 1.78$ ,  $q = 0.69$  and  $V_0 = 6.73 \text{ cm}^3/\text{mol}$ .

The  $P, T$  description of  $\gamma$  is expressed in a polynomial form

$$\gamma(P, T) = \frac{a + cP + eT + gP^2 + iT^2 + kPT}{1 + bP + dT + fP^2 + hT^2 + jPT} \quad (S2)$$

We described  $K_T(P, T)$  by the following equation

$$K_T(P, T) = K_1 + \frac{K_2 P}{\ln(P)} + \frac{K_3 T}{\ln(T)} \quad (S3)$$

All the coefficients for  $\gamma$  and  $K_T$  (Eqs. S2 and S3) are given in Extended Data Table 2.

This model gives good agreement with  $\epsilon$ -Fe electrical resistivity data at lower pressures and ambient temperatures<sup>5,14</sup>, fits the present thermal conductivity results on  $\epsilon$ -Fe well (Fig. 2), and implies thermal conductivity is only weakly pressure

dependent above 100 GPa, consistent with prior expectations<sup>2</sup>. Thus, our measurements, taken at pressures close to those at the top of Earth's core, should constrain overall core conductivity accurately.

### The Lorenz Number for $\epsilon$ -Fe

The temperatures and pressures of our thermal conductivity measurements overlap with those of shock wave electrical resistivity measurements<sup>15</sup>, allowing a comparison between the resistivity and thermal conductivity measurements to obtain an empirical value for  $L$ .

At 112 GPa, where the most extensive high temperature dataset was available in the present results, electrical conductivity was estimated as follows using the data of Bi et al.<sup>15</sup>. The two lowest pressure points from that study at 101.1 GPa and 146.7 GPa are solid-state data and so are comparable to the present results; a higher pressure point corresponds to the liquid<sup>15,18</sup>. First, a temperature for the middle of the 3 data points (146.7 GPa, 3357 K) after isentropic release from the initial conditions (173.4 GPa, 3552 K), not reported, was estimated from the scaling of release behaviour reported by Bi et al.; release temperatures were confirmed by independent calculation using an  $\epsilon$ -Fe equation of state<sup>34</sup>. The electrical conductivity at 112 GPa is then estimated as  $1.13(11) \times 10^6$  S/m at 2332 K, based on a linear interpolation between the solid-state data points, and assuming an uncertainty of  $\sim 10\%$  consistent with the uncertainty typically reported in this type of measurement<sup>16</sup> and the scatter in the data reported by Bi et al. At this temperature in our experiments,  $k = 50 \pm 10$  W/m/K (Fig. 3). Then the corresponding value of  $L$  is  $1.9 \pm 0.4 \times 10^{-8}$  W $\Omega$ K<sup>-2</sup>, or a reduction of  $22 \pm 16\%$  from the standard value for a free electron metal. This correction has a small influence on our results, as use of the free-electron value of  $L$  on prior resistivity experiments produces Fe thermal conductivities only slightly above the values

determined here. For example, assuming the free-electron value of  $L$ , the shock wave results of Bi et al.<sup>15</sup> imply the value of 67 W/m/K at 112 GPa and 2330 K, compared to our model value of 41 W/m/K.

The correction to the standard value of  $L$  determined here for  $\epsilon$ -Fe is typical for Fe at various conditions and phases<sup>7,14,24,44</sup> ( $\pm 30\%$ ) and is similar to other transition metals<sup>11,45</sup>. In Pt,  $L$  is measured<sup>11</sup> to deviate from the ideal value by  $\pm 30\%$  at temperatures up to 2000 K. For Mo, deviations of -10 to -30% are predicted at high temperature<sup>45</sup>. The variation of  $L$  across transition metals at low temperature alone is large<sup>46</sup>, with values such as in Cu (-9%) and W (+31%).

We note that an early conference proceedings reporting shock data on Fe electrical resistivity at high pressures<sup>16</sup>, corresponding to systematically higher electrical conductivities compared to later work<sup>15</sup> cannot be considered to agree with our measurements, as an unrealistically large reduction in the Lorenz number would be needed. It has been proposed that spurious values were obtained in the earlier studies at higher pressure ( $P > 50$  GPa) due to insulator-conductor transformation of epoxies intended for use as insulators in target construction, an effect avoided in later measurements<sup>15</sup>.

### Model for temperature variation of thermal conductivity

Eq. 2 (main text) was selected in consideration of the observed variation of electrical conductivity in  $\epsilon$ -Fe with temperature<sup>5,14</sup>. Electrical conductivity is modelled as following a relationship

$$\sigma = \sigma_0 + AT^n \quad (S4)$$

where  $n = -1$  is typically assumed for metals at high temperatures as in the Bloch-Grüneisen model<sup>5,7,13,14</sup>. A value closer to  $n = -1.3$  has been suggested for Fe at high pressures from resistivity measurements under shock and static loading probing temperatures and pressures similar to those examined here<sup>14</sup>. Similarly, fitting Eq. S4 to resistivity data under high pressure external heating<sup>5</sup>, for which temperatures are particularly accurate, yielded values of  $n = -1.50 \pm 0.07$ ,  $\sigma_0 = 1.04 \pm 0.46 \times 10^6$ ,  $A = 6.51 \pm 2.2 \times 10^{10}$ , for  $\sigma$  in S/m and  $T$  in K (Extended Data Fig. 1a).

Then, in consideration of the Wiedemann-Franz relation (Eq. 1)

$$k = LT\sigma$$

we can write

$$k = L(T\sigma_0 + AT^{1+n}) \quad (S5)$$

leading to the empirical form in Eq. 2. We chose here  $n=-1.5$ , though results are not significantly different selecting  $n=-1.3$ , or similar.

Eq. 2 is fit to the present measurements at 112 GPa together with shock wave resistivity data<sup>15</sup>, interpolated to 112 GPa as discussed above, and static resistivity data<sup>5,14</sup> extrapolated to 112 GPa using a double-exponential fit of the form

$$\frac{1}{\sigma} = \alpha + \beta_1 \exp(\tau_1 P) + \beta_2 \exp(\tau_2 P) \quad (S6)$$

An initial fit gave  $a = 0.89 \pm 1.33 \times 10^{-3} \text{ W/m/K}^2$ ,  $b = 2040 \pm 140 \text{ W/m/K}^{1/2}$ . The linear component of the fit is nearly zero, whereas the inverse square term is strongly nonzero. Thus a reasonable simplified version of this model for Fe is

$$k = b'/\sqrt{T} \quad (S7)$$

where  $b = 1972 \pm 83 \text{ W/m/K}^{1/2}$  (Fig. 3 and Extended Data Fig. 1b).

The model captures a decrease in the thermal conductivity with temperature, which is seen in the present measurements and also implied by the prior resistivity data<sup>5,14,15</sup> (Fig. 3). In terms of electrical resistivity (Extended Data Fig. 1c), the scaling with temperature obtained by the model compares well with that observed by Gomi et al.<sup>5</sup> in  $\epsilon$ -Fe at lower pressures, and shows a similar dependence to that seen in  $\gamma$ -Fe (or possible  $\gamma$ - $\epsilon$  mixed phase) at high temperatures<sup>21</sup>. It is seen that  $\epsilon$ -Fe up to 112 GPa has higher resistivity than  $\gamma$ -Fe (or its mixed phase) at lower pressure (Extended Data Fig. 1c), consistent with our experimental observation of higher thermal conductivity in  $\gamma$ -Fe compared to  $\epsilon$ -Fe in the low pressure region (Fig. 2).

We note that the minimum measured thermal conductivity is in close agreement with values expected at traditional resistivity saturation<sup>5</sup> (Extended Data Fig 1b), however, as resistivity saturation in Fe at extremes has not been clearly confirmed by theoretical studies and since available saturation models<sup>5</sup> cannot satisfactorily describe the data, we conclude that at present there is no reason to conclude resistivity saturation has occurred. Assuming it has, then  $\epsilon$ -Fe at temperatures above  $\sim 3000 \text{ K}$  is saturation-dominated, such that thermal conductivities at core conditions would be somewhat higher (60-80 W/mK) than assessed by the present modelling; however, this upper bound on conductivity is still low compared to many prior estimates, and would not substantially alter our main conclusions.

#### Error assessment in the thermal conductivity determination

Use of the laser-heated DAC in combination with numerical simulations has been shown to represent a promising tool for studying heat transfer at high pressures and temperatures<sup>11,12,26,30,47-50</sup>. This approach requires a detailed understanding of heat

transfer in the DAC, including quantitative relationships between the temperature distribution, pressure chamber geometries and sample physical properties.

Fitting was generally performed using a manual adjustment of model parameters. This approach was evaluated against a Levenberg-Marquardt least-squares minimisation of the finite element model variables (Extended Data Fig. 5). This automatic optimisation was able to improve fit quality however the improvement was not statistically significant. Furthermore, as a good initial guess was required, this additional step only added to the processing time, so was not used for all datasets.

In the present study, all input parameters in finite-element modelling were carefully examined for their effect on the determination of sample thermal conductivity (Extended Data Figs 2 and 3). Uncertainties in the input parameters (such as pressure chamber geometry) were in this way included in our overall uncertainty determination for  $k$ .  $C_p$  of the pressure medium has negligible effect (Extended Data Fig. 3a). For  $C_p$  of iron we derived a range of values of 500-700 J/kg/K from equations of state for  $\epsilon$ -Fe<sup>34,51</sup> and other estimates<sup>52</sup>. Within this range, resulting sample  $k$  is unaffected (Extended Data Fig. 3b). Thermal conductivity of the diamond anvils, temperature dependence of thermal conductivity of the pressure medium, and smaller or larger laser beam size (by about 13%) have also negligible effect on the sample  $k$  (Extended Data Fig. 3c-e). Sample and insulation layer thicknesses, on the other hand, contribute to the uncertainty in sample  $k$  – approximately  $\pm 20\%$  change in thicknesses leads to  $\pm 7$  W/m/K changes in sample  $k$  (Extended Data Fig. 3f-i). We assume a constant value of  $k$  for the foil in our simulations, but this produces no significant change in results compared to a temperature dependent  $k$  (Extended Data Fig. 3j).

To check potential couplings between the uncertainties in the input parameters, we have also propagated uncertainty in our input parameters in a more rigorous manner using a Monte-Carlo approach (Extended Data Fig. 6). To do this, we considered only parameters which were identified as having a significant impact on the measurements: the thicknesses of the medium on both sides of the sample, and the sample thickness. We performed 64 Monte Carlo samples within the Gaussian probability distributions of the thickness parameters, given standard deviations of 30% in each, for a representative experiment at 130 GPa (See Extended Data Fig. 6a). For each sampling, the data was fitted automatically (Extended Data Fig. 5) to determine the two thermal conductivities and the powers for the three lasers (Extended Data Fig. 6b). The distribution in these values has a standard deviation comparable to our single-point error for  $k_{Fe}$  (Extended Data Fig. 6d).

While suitably sensitive to the thermal conductivity of the foil, our measurements are less sensitive to the thermal conductivity of the insulating medium, which is included as a variable in fitting (usually as a constant) but which had values more sensitive to the assumed sample geometry (thickness of the insulation layers), laser beam diameter and laser power. Thus, conductivities of insulating media are not reported, as they are not robustly determined by our approach. For Ar, the values of  $k$  obtained in the fits were generally in the range of 50-100 W/m/K, consistent with previously reported values<sup>49</sup>.

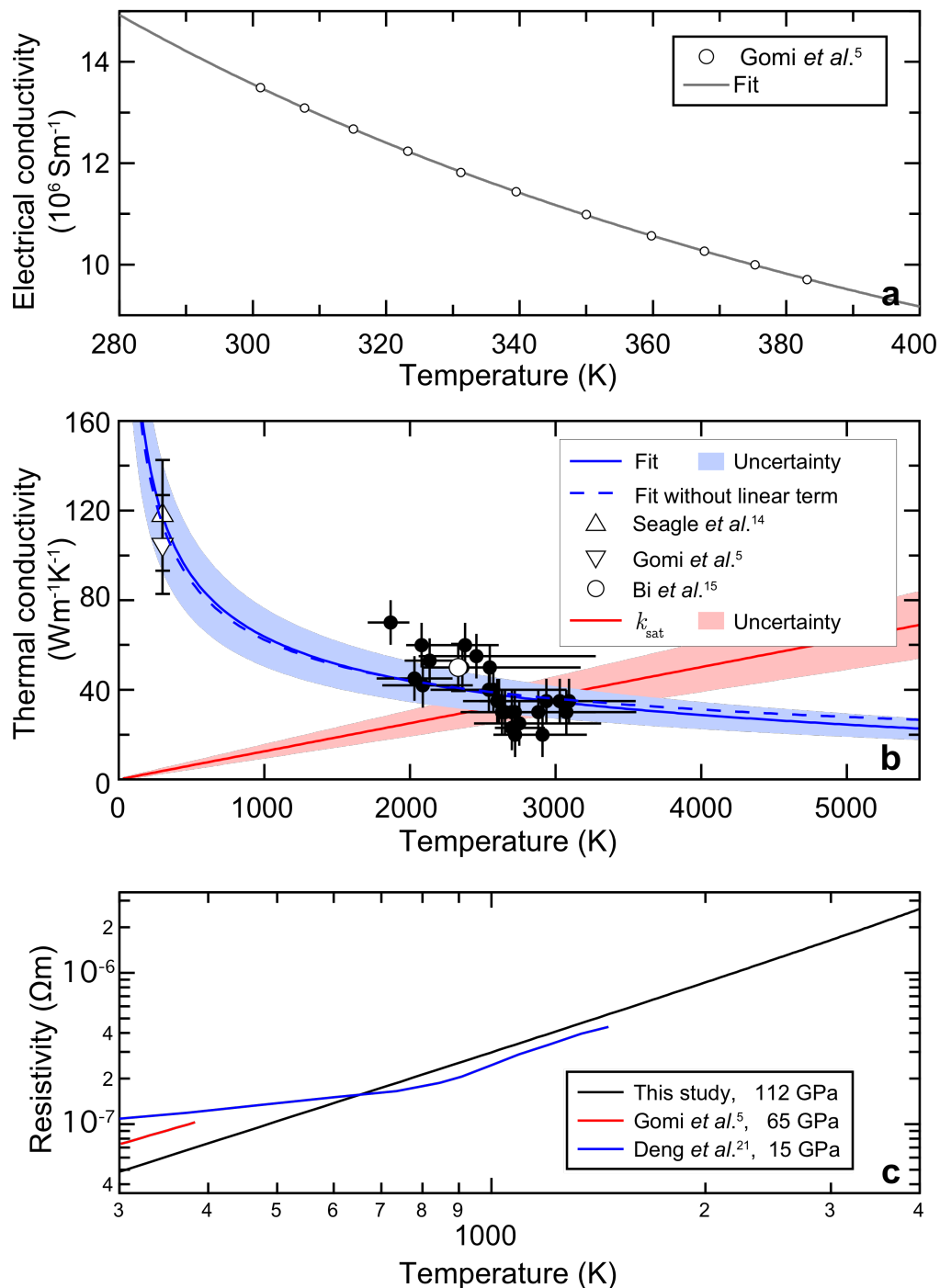
## METHODS REFERENCES

- 30 Montoya, J. A. & Goncharov, A. F. Finite element calculations of the time dependent thermal fluxes in the laser-heated diamond anvil cell. *J. Appl. Phys.* **111**, 9 (2012).
- 31 Johannsen, P. G. Refractive index of the alkali halides .1. Constant joint density of states model. *Physical Review B* **55**, 6856-6864 (1997).
- 32 Grimsditch, M., Letoullec, R., Polian, A. & Gauthier, M. Refractive index determination in diamond anvil cells: Results for argon. *J. Appl. Phys.* **60**, 3479-3481 (1986).
- 33 Chen, B. *et al.* Elasticity, strength, and refractive index of argon at high pressures. *Physical Review B* **81**, 144110 (2010).
- 34 Dewaele, A. *et al.* Quasihydrostatic Equation of State of Iron above 2 Mbar. *Physical Review Letters* **97**, 215504 (2006).
- 35 Sommerfeld, A. Zur Elektronentheorie der Metalle auf Grund der Fermischen Statistik. *Z. Physik* **47**, 1-32 (1928).
- 36 Parker, W. J., Jenkins, R. J., Abbott, G. L. & Butler, C. P. Flash method of determining thermal diffusivity, heat capacity, and thermal conductivity. *J. Appl. Phys.* **32**, 1679 (1961).
- 37 Tateno, S., Hirose, K., Ohishi, Y. & Tatsumi, Y. The structure of iron in Earth's inner core. *Science* **330**, 359-361 (2010).
- 38 Shen, G., Prakapenka, V. B., Rivers, M. L. & Sutton, S. R. Structure of Liquid Iron at Pressures up to 58 GPa. *Physical Review Letters* **92**, 185701 (2004).
- 39 Goncharov, A. F. *et al.* X-ray diffraction in the pulsed laser heated diamond anvil cell. *Review of Scientific Instruments* **81**, 113902 (2010).

- 40 Ross, R. G., Andersson, P., Sundqvist, B. & Backstrom, G. Thermal conductivity of solids and liquids under pressure. *Reports on Progress in Physics* **47**, 1347 (1984).
- 41 Bohlin, L. Thermal conduction of metals at high pressure. *Solid State Commun.* **19**, 389-390 (1976).
- 42 Sharma, S. K. Debye temperature of hcp iron at extreme compression. *Solid State Commun.* **149**, 2207-2209 (2009).
- 43 Dubrovinsky, L. S., Saxena, S. K., Dubrovinskaia, N. A., Rekh, S. & Le Bihan, T. Gruneisen parameter of  $\epsilon$ -iron up to 300 GPa from in-situ X-ray study. *American Mineralogist* **85**, 386-389 (2000).
- 44 Van Zytveld, J. Electrical Resistivities of Liquid Transition Metals. *Journal de Physique Colloques* **41**, C8-503-C508-506 (1980).
- 45 French, M. & Mattsson, T. R. Thermoelectric transport properties of molybdenum from ab-initio simulations. *Physical Review B* **90**, 165113 (2014).
- 46 Kittel, C. *Introduction to Solid State Physics*. 8th edn. (John Wiley & Sons, 2005).
- 47 Panero, W. R. & Jeanloz, R. Temperature gradients in the laser-heated diamond anvil cell. *Journal of Geophysical Research: Solid Earth* **106**, 6493-6498 (2001).
- 48 Kiefer, B. & Duffy, T. S. Finite element simulations of the laser-heated diamond-anvil cell. *J. Appl. Phys.* **97**, 114902 (2005).
- 49 Goncharov, A. F. *et al.* Thermal conductivity of argon at high pressures and high temperatures. *J. Appl. Phys.* **111** (2012).

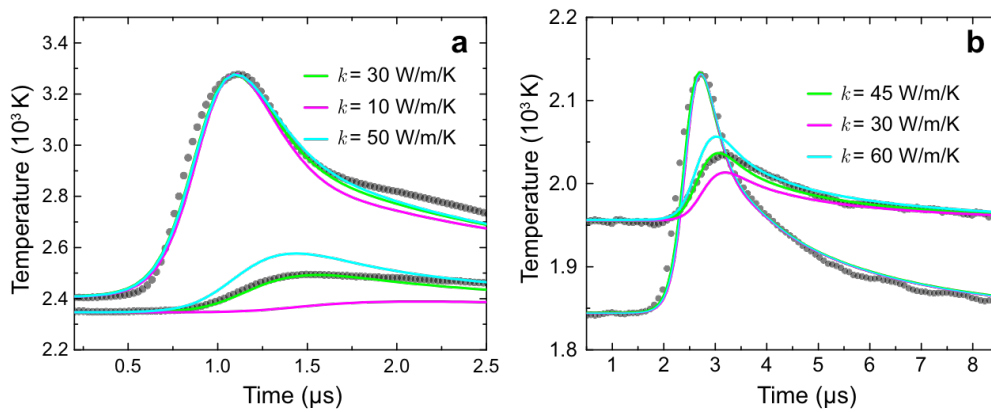
- 50 Beck, P. *et al.* Measurement of thermal diffusivity at high pressure using a transient heating technique. *Applied Physics Letters* **91**, 181914 (2007).
- 51 Yamazaki, D. *et al.* P-V-T equation of state for  $\epsilon$ -iron up to 80 GPa and 1900 K using the Kawai-type high pressure apparatus equipped with sintered diamond anvils. *Geophysical Research Letters* **39**, L20308 (2012).
- 52 Hirose, K., Labrosse, S. & Hernlund, J. Composition and State of the Core. *Annual Review of Earth and Planetary Sciences* **41**, 657-691 (2013).

EXTENDED DATA LEGENDS

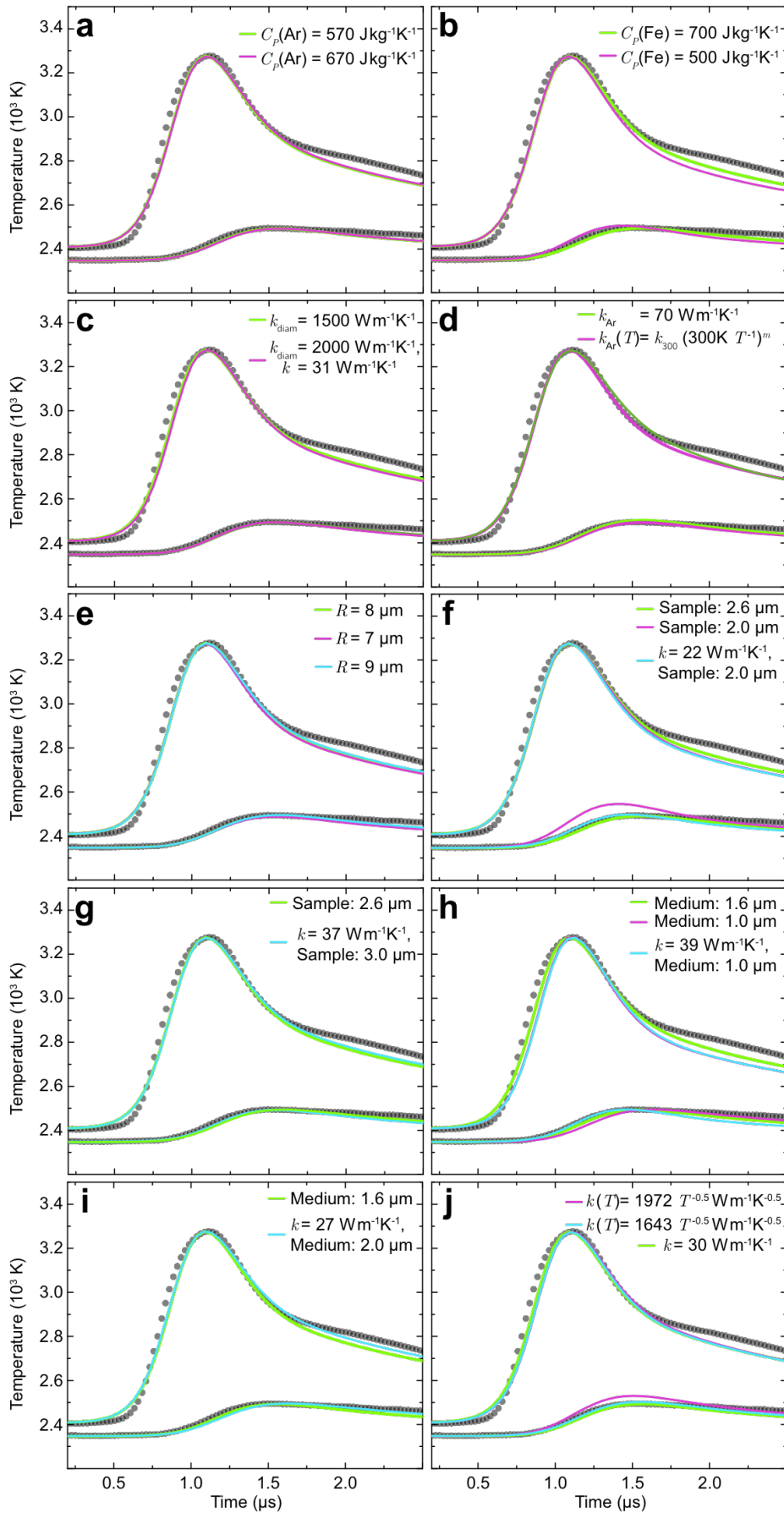


EXTENDED DATA FIG. 1. High temperature transport properties of Fe. a, Graph of the electrical conductivity<sup>5</sup> as function of temperature of  $\epsilon$ -Fe at 65 GPa and model fit (to Eq. S4, Methods). b, Thermal conductivity temperature dependence at 112 GPa.

Model fit (to Eq. 2, solid line) and a 20% uncertainty envelope are in blue; model fit without linear term (to Eq. S7, Methods) is dashed blue line. Present data are solid circles and data derived from prior electrical resistivity measurements<sup>5,14,15</sup> are open symbols (see Fig. 3). Red band is the minimum thermal conductivity assuming resistivity saturation<sup>5</sup>. c, Electrical resistivity at several pressures, for multiple phases at 15 GPa (blue)<sup>21</sup>, and the  $\epsilon$  phase at 65 GPa (red)<sup>5</sup> and 112 GPa (this study, black).

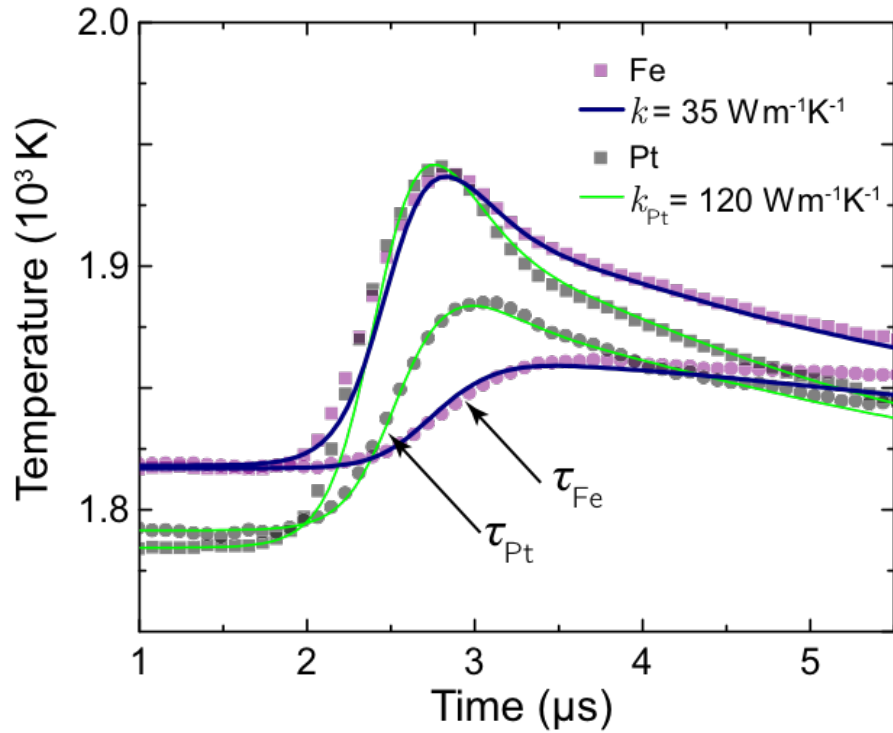


EXTENDED DATA FIG. 2: Example of measured temperatures as a function of time from the pulsed and opposite sides of the foil (dots). Green, magenta and cyan curves are simulations with different values of sample  $k$ , all other parameters being held constant. The datasets at 112 GPa (a) and 130 GPa (b) have been measured using 3 and 10  $\mu$ s sweep windows, respectively.

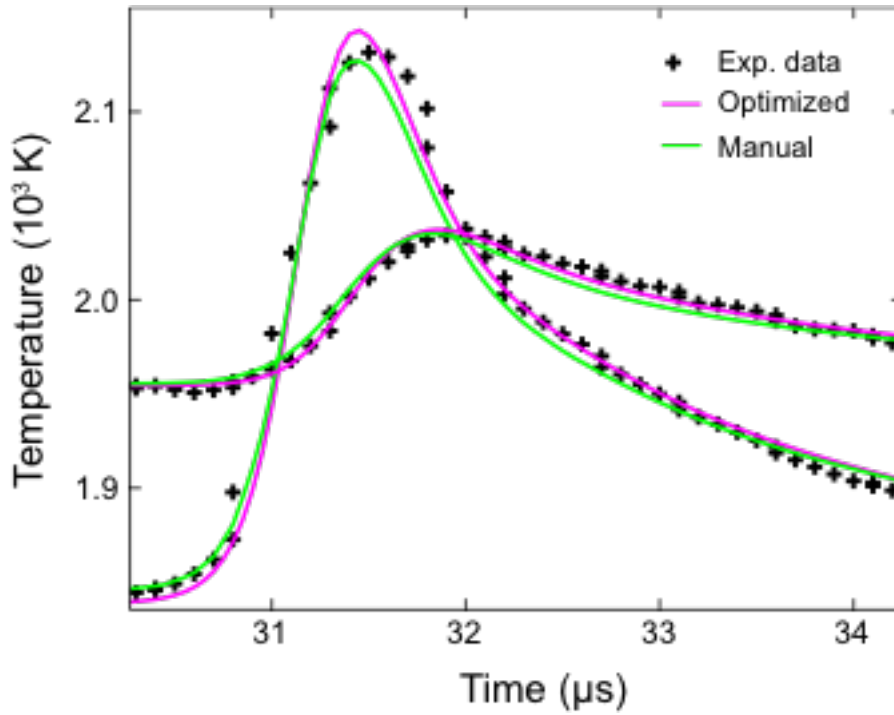


EXTENDED DATA FIG. 3: Tests of the sensitivity of finite element model results to input parameters for an example run at 112 GPa. This experiment shows a large amplitude of temperature modulation that accentuates the effects of parameter changes. A best fit value of  $k = 30$  W/m/K, obtained using parameters listed in Extended Data Table 1, is obtained from these model fits unless stated otherwise. a, Effect of heat capacity of the Ar pressure medium. Uncertainty in medium  $C_P$  has no effect on  $k$  of the sample. b, Effect of heat capacity of the sample. Temperature profiles for two values of  $C_P$  of Fe (500 and 700 J/kg/K) indicate that results are only weakly affected by uncertainty in  $C_P$  of Fe. c, Change in thermal conductivity value of diamond anvils from 1500 to 2000 W/m/K requires increase in thermal conductivity of the sample from 30 to 31 W/m/K. d, Effect of using a  $T$ -dependent  $k$  of medium. After Ref. <sup>49</sup>, a dependence  $k(T) = k_{300}(300/T)^m$  is used, where  $k_{300}$  is the 300 K conductivity,  $T$  is in K, and  $m$  is an exponent (of order 1);  $k_{300}$  is extrapolated from prior results at lower pressure<sup>49</sup> and  $m$  is fit to the present data. No change in sample  $k$  is indicated using this or any other  $k(T)$  model we tested for the media. e, Laser beam radius change of  $\pm 13\%$  does not affect the temperature profile significantly. f, Thinner sample by 23% (from 2.6 to 2.0  $\mu\text{m}$ ) would require lower sample  $k$  of 22 W/m/K. g, Thicker sample by 15% (from 2.6 to 3.0  $\mu\text{m}$ ) would require increased sample  $k$  of 37 W/m/K. h, Insulation layer was decreased on both sides by 38%, from 1.6  $\mu\text{m}$  to 1.0  $\mu\text{m}$ . Sample  $k$  had to increase to 39 W/m/K. i, Insulation layer was increased on both sides by 25%, from 1.6  $\mu\text{m}$  to 2.0  $\mu\text{m}$ . Sample  $k$  decreased to 27 W/m/K. j, Effect of including  $T$  dependence of sample  $k$  in models. In magenta is temperature profile calculated using our global fit at 112 GPa (Eq. 2); in cyan is this dependence scaled within its uncertainty (reduced by a factor of 0.83) to improve the fit. The resulting sample  $k$  varies between 24 and 35 W/m/K in the  $T$

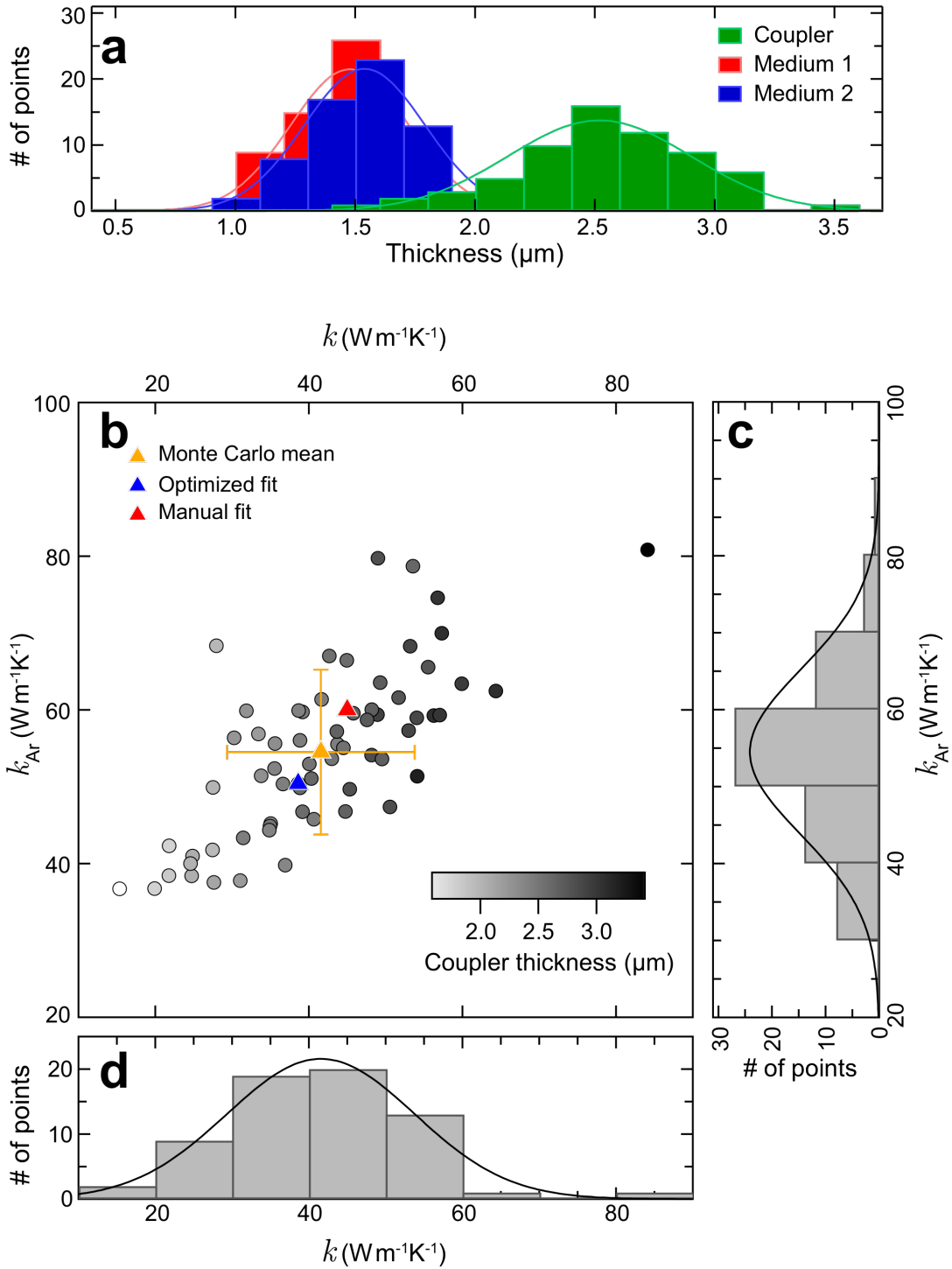
range of the experiment; the estimate assuming constant sample  $k$  is the average of these values.



EXTENDED DATA FIG 4. Comparison between data on Fe and Pt at 48 GPa showing clearly slower propagation of heat across the Fe foil compared to Pt<sup>11</sup>, as given by the half-rise time  $\tau$ . This observation directly shows that thermal diffusivity  $\kappa=(k/\rho C_P)$  of Fe is much less than Pt, since<sup>11,36</sup>  $\kappa \sim 1/\tau$ . Similarly, the smaller amplitude of the perturbation upon opposite surface arrival indicates smaller  $k$  in Fe compared to Pt.



EXTENDED DATA FIG 5. Comparison between manual and automatic optimisation results for an experiment at 130 GPa. The manual approach, used as our primary fitting method, was based on an adjustment of model parameters by hand within a precision of  $\sim 5$  W/m/K, giving  $k_{\text{Fe}}=45$  W/m/K and  $k_{\text{Al}}=60$  W/m/K as the best fit. The automatic result is the best fit based on a Levenberg-Marquardt least squares minimisation of model parameters, yielding  $k_{\text{Fe}}=38.6$  W/m/K and  $k_{\text{Al}}=50.4$  W/m/K. The automatic optimization obtained a better least squares fit ( $\chi^2$  improved by 23%), however the difference in  $k_{\text{Fe}}$  is not statistically significant.



EXTENDED DATA FIG 6. Monte-Carlo (MC) analysis of error coupling due to sample thickness and effect on thermal conductivities, for 130 GPa dataset shown in Extended Data Fig. 5. **a** Histogram showing randomly sampled thicknesses (upper and lower medium, and foil) in Gaussian probability distributions with standard

deviation 30%. **b** Thermal conductivities for argon and iron for 64 samples. The grey scaled colour refers to the value of the coupler thickness showing the correlation between high values for  $k_{Fe}$  and thicker coupler. The results of fits shown in Extended Data Fig. 5 are blue and red triangles, while the mean and 1-sigma standard deviation found from the spread of sampled thermal conductivities is the orange triangle. **c** and **d** are histograms showing the distribution of thermal conductivities in **b**.

$P$ (GPa)	medium	sample thickness ( $\mu\text{m}$ )	pulsed side thickness ( $\mu\text{m}$ )	opposite side thickness ( $\mu\text{m}$ )	medium density ( $\text{kg m}^{-3}$ )	$C_p$ , medium ( $\text{J kg}^{-1}\text{K}^{-1}$ )	iron density ( $\text{kg m}^{-3}$ )	$C_p$ , iron ( $\text{J kg}^{-1}\text{K}^{-1}$ )
35	NaCl	3.0	8.0	7.0	3630	$\left\{ \begin{array}{l} 748 + 0.34 T, \quad T < 1000\text{K} \\ 1103, \quad T > 1000\text{K} \end{array} \right.$	9602	450
48	NaCl	2.9	7.4	6.7	3911		$\left\{ \begin{array}{l} 748 + 0.34 T, \quad T < 1000\text{K} \\ 1103, \quad T > 1000\text{K} \end{array} \right.$	9929
58	Ar	2.9	1.5	6.5	4539	570	10174	700
74	Ar	2.8	1.0	6.4	4800	570	10476	700
88	Ar	2.7	1.7	1.7	5057	570	10800	700
112	Ar	2.6	1.6	1.6	5326	570	11225	700
130	Ar	2.5	1.5	1.5	5550	570	11590	700

EXTENDED DATA TABLE 1: Input parameters used for the finite element modelling.

	Coefficient for Grüneisen parameter	Coefficient for $K_T$
$a$	$1.76 \times 10^0$	$K_1$ 97.50
$b$	$2.04 \times 10^{-2}$	$K_2$ 25.77
$c$	$2.90 \times 10^{-2}$	$K_3$ -0.26
$d$	$-1.32 \times 10^{-4}$	
$e$	$-1.87 \times 10^{-4}$	
$f$	$3.90 \times 10^{-5}$	
$g$	$3.42 \times 10^{-5}$	
$h$	$2.55 \times 10^{-9}$	
$i$	$3.05 \times 10^{-9}$	
$j$	$-5.10 \times 10^{-7}$	
$k$	$-4.37 \times 10^{-7}$	

EXTENDED DATA TABLE 2: Coefficients for Grüneisen parameter and isothermal bulk modulus used to estimate pressure variation of thermal conductivity.